Key Points:
- We use X-ray computed tomography to visualize the pore space and nonwetting phase during two-phase flow experiments in three sandstones
- Persistent homology characterizes size, distribution, and frequency of important pore space and nonwetting fluid topological features in 3-D
- Metric derived from persistent homology correlates with nonwetting fluid trapping for all sandstone types and saturations

Topological Persistence for Relating Microstructure and Capillary Fluid Trapping in Sandstones

A. L. Herring[1] , V. Robins[1] , and A. P. Sheppard[1]

[1]Department of Applied Mathematics, Research School of Physics and Engineering, Australian National University, Canberra, ACT, Australia

Abstract Results from a series of two-phase fluid flow experiments in Leopard, Berea, and Bentheimer sandstones are presented. Fluid configurations are characterized using laboratory-based and synchrotron based 3-D X-ray computed tomography. All flow experiments are conducted under capillary-dominated conditions. We conduct geometry-topology analysis via persistent homology and compare this to standard topological and watershed-partition-based pore-network statistics. Metrics identified as predictors of nonwetting fluid trapping are calculated from the different analytical methods and are compared to levels of trapping measured during drainage-imbibition cycles in the experiments. Metrics calculated from pore networks (i.e., pore body-throat aspect ratio and coordination number) and topological analysis (Euler characteristic) do not correlate well with trapping in these samples. In contrast, a new metric derived from the persistent homology analysis, which incorporates counts of topological features as well as their length scale and spatial distribution, correlates very well ($R^2 = 0.97$) to trapping for all systems. This correlation encompasses a wide range of porous media and initial fluid configurations, and also applies to data sets of different imaging and image processing protocols.

Plain Language Summary When fluids flow through porous rocks or soils, small bubbles ("ganglia") of oil or gas may become trapped in the pore structure of the rock. This occurs during many natural and engineered processes (e.g., rainfall infiltration into soils, enhanced oil recovery, geologic carbon dioxide sequestration, contaminant remediation of pollutants in soils). In this study, we analyze the small-scale 3-D structure (length scales on the order of microns) of sandstone rocks to determine the structural controls on ganglion trapping, and compare to results from a series of fluid flow experiments. The analysis uses a new data/image analysis technique known as "persistent homology" that can quantify structure in terms of geometry, topology, and spatial distribution. We define a new metric which combines these structural impacts and demonstrate that the new metric provides a universal correlation for ganglia trapping levels for a variety of sandstone types and initial fluid configurations, and also applies to 3-D data sets derived from different imaging and image processing protocols.

1. Introduction

Accurate modeling and design of engineered subsurface operations requires knowledge of system properties spanning multiple length scales. Reservoir or basin-scale processes (kilometer-scale) are dependent on porous medium microstructure (micron-scale). For systems containing two or more fluid phases, the pore-scale distribution of fluids (including submicron fluid films on pore walls) has a critical influence on the larger-scale flow, transport, and chemical interactions.

The interfacial interactions between the solid surface and the fluids determine the arrangement of fluids within the pore space. In a strongly wetting media, the solid surface exhibits a strong affinity for one fluid (termed the "wetting" fluid) over the other ("nonwetting" fluid), with the result that the wetting fluid covers the solid surface of the media and is tightly held within the small crevices of the solid. Considerable research effort has been made to describe the complicated arrangement of fluids under a range of conditions, including efforts to quantify saturation levels, fluid–fluid pressure differences, fluid–fluid interfacial areas, and fluid connectivity (Cheng, 2004; Culligan et al., 2004; Dalla et al., 2002; Gray et al., 2015; McClure et al., 2016; Porter et al., 2009, 2010).

One area of active research in the multiphase flow community deals with how to predict and manipulate levels of nonwetting phase trapping during flow processes. Nonwetting phase trapping, often termed

"capillary trapping" or "residual trapping," is a function of the geometry of the solid medium architecture as well as the fluid properties. Once nonwetting phase is present in a medium, it may become isolated and trapped within the pore bodies of the medium during local imbibition processes: as wetting phase saturation increases and films thicken, the films may merge at medium constrictions (throats), thereby "snapping-off" and isolating nonwetting phase ganglia (e.g., Chatzis et al., 1983; Morrow et al., 1988; Roof, 1970). Although snap-off is commonly thought of as a process occurring during imbibition, recent experimental studies have demonstrated that the phenomenon occurs intermittently during drainage as well (Andrew et al., 2015; Bultreys et al., 2015; Herring et al., 2018; Reynolds et al., 2017; Singh et al., 2017). Accurate estimation of trapped, nonmobile, nonwetting phase fluid in the subsurface is a critical parameter for engineering processes such as enhanced oil recovery, geologic CO_2 sequestration, and contaminant remediation. To this end, many previous studies have attempted to link trapping levels to porous media structural characteristics (e.g., Chatzis & Morrow, 1984; Li & Wardlaw, 1986b; Wardlaw & Li, 1988), in addition to fluid–fluid interactions (e.g., Bennion & Bachu, 2013; Kimbrel et al., 2015; Morrow et al., 1988) and dynamic influences (Deng et al., 2015; Singh et al., 2017).

Using network statistics approaches, two structural metrics have been identified as predictors of snap-off: pore body-throat aspect ratios and pore coordination numbers. Aspect ratio measures the relative length scales of pore bodies and throats (e.g., pore body diameter divided by pore throat diameter); given the description of snap-off above, it is intuitive that large aspect ratios facilitate high levels of nonwetting phase trapping, while aspect ratios near unity suppress snap-off (Mahmud & Nguyen, 2006; Nguyen et al., 2006; Wardlaw & Li, 1988). Coordination number measures the number of pore throats connected to a given pore body; it has been proposed that a higher coordination number leads to higher trapping of nonwetting phase, as more pore throats provide more opportunities for wetting fluid to bypass nonwetting ganglia (Al-Raoush & Willson, 2005; Tanino & Blunt, 2012).

An alternative method (in contrast to network statistic-based approaches) to describe the pore-scale arrangement of solid and fluid phases within porous media is to compute topological invariants (Herring et al., 2013, 2015; Mecke & Arns, 2005; Mecke & Wagner, 1991; Vogel, 2002; Vogel et al., 2010; Vogel & Kretzschmar, 1996). In this approach, topology is typically quantified via the Euler characteristic, which is defined as the alternating sum of Betti (β) numbers:

$$\chi = \beta_0 - \beta_1 + \beta_2 \tag{1}$$

Here β_0 is the number of discrete objects present in the volume; β_1 is the number of redundant connections, or loops, within the objects; and β_2 is the number of cavities within the objects.

For porous media applications, two sets of topologies are relevant: the topology of the pore space of the medium and the topology of the fluid phases which reside within the pore space. Accurate visualization and sufficient resolution is required to adequately measure topological features. For many visualization studies, fluid and solid phase locations are measured via 3-D X-ray microcomputed tomography (CT) with image (voxel) resolution on the order of 1–10 μm (Wildenschild & Sheppard, 2013). This "micro" scale imaging allows for visualization of sample sizes large enough to comprise representative volumes for many consolidated geologic materials, while still resolving the distribution of solid and pore space, and the nonwetting phase within the pore space. Wetting phase films, however, are too thin to be captured via this imaging scale (although wetting films have been observed in other experimental systems with higher resolution techniques (Kazemifar et al., 2015; Kim et al., 2012)). Due to the inherent competition between increasing resolution and maximizing sample size, the topology of the wetting phase has not been measured for sample sizes large enough to be considered representative. However, topology of the nonwetting phase (which does not form thin films) has been successfully measured in geologic systems (e.g., Herring et al., 2013).

In the context of the nonwetting fluid within a porous medium, β_0 is the number of individual nonwetting fluid bubbles or ganglia within the analyzed volume, β_1 is the number of redundant pore throats through which the nonwetting ganglia are interconnected, and β_2 would indicate solid or wetting phase floating within the nonwetting phase (thus, β_2 is generally not relevant for characterizing nonwetting phase). A multiphase-porous medium system with a high saturation of nonwetting phase exhibits a large negative Euler characteristic value (large β_1 value) as the nonwetting phase enters into the many small pore throats

connected to the larger pore bodies, creating large numbers of redundant loops and enhancing the interconnectivity of the nonwetting phase within the pore space. Alternatively, a multiphase-porous medium system which contains a lower saturation level of capillary-trapped nonwetting phase, for example, nonwetting phase which is only present in pore bodies as isolated bubbles or ganglia surrounded and trapped by wetting fluid, will have a positive Euler value (i.e., large β_0 value). Between these two extremes, the Euler characteristic will generally become more negative during drainage, as nonwetting phase invades pore throats and becomes more interconnected, and will become more positive during imbibition, and wetting phase flows into the medium and snaps off nonwetting phase into isolated clusters. An Euler number near 0 typically indicates that the nonwetting fluid phase is near the percolation threshold of the pore space and thus near the limit of capability for flow from one end to the other through the analyzed volume (Mecke & Arns, 2005).

With this understanding, researchers have recently used nonwetting phase topology to describe fluid distributions (Herring et al., 2016; Khanamiri & Torsaeter, 2018), linked topology to relative permeability (Liu, Herring, Arns, et al., 2017), used nonwetting phase topology to describe fluid flow regimes (Schlüter et al., 2016) and fluid displacement mechanisms during dynamic processes (Armstrong et al., 2016; Rücker et al., 2015), and proposed that nonwetting phase topology is a metric previously missing from thermodynamic models of multiphase flow (McClure et al., 2016). With respect to nonwetting phase trapping and mobilization, Herring et al. (2013, 2015) observed that Bentheimer sandstone samples with more highly interconnected nonwetting phase fluid ganglia (large β_1 values) exhibited reduced trapping (enhanced mobilization) during subsequent imbibition processes; the relationship observed in that study was proposed to provide a physical mechanism for the characteristic shape of the "trapping curve," the commonly used empirical relationship that links initial nonwetting fluid saturation and residual trapped fluid saturation (see, e.g., Al Mansoori et al., 2010; Land, 1968).

While topology is a powerful tool to describe fluid distributions, topological metrics, by definition, provide information on the *connectivity* of a phase, not the geometry (shape or size). Similarly, network statistics approaches provide distributions of local pore-throat geometries and configurations, but these local measures contain no global information. Physical flow characteristics, that is, the permeability or trapping of a fluid phase, are dependent on both connectivity of the pore space or fluid phase as well as size of connections.

Persistent homology provides a method to link measurement of topological features to the length scales of the features (Delgado-Friedrichs et al., 2015; Edelsbrunner et al., 2002; Robins, 1999). Persistent homology has been used to investigate the length scales of connectivity for a wide range of applications, including in neuroscience (Dabaghian et al., 2012), materials informatics (Lee et al., 2017), granular materials (Saadatfar et al., 2017), fluid dynamics (Kramar et al., 2016), and time series analysis (Sanderson et al., 2017). Persistent homology analysis provides a method to measure the important characteristics of porous medium topology in combination with their size and distribution, potentially combining the advantages of the topology and network statistics approaches.

In this study, we apply persistent homology analysis to a series of new two-phase fluid flow experiments (air and brine drainage imbibition) in a variety of water-wet sandstones, conducted under low capillary number conditions. Experiments were visualized with 3-D X-ray micro CT. The persistent homology analysis provides quantification of the occurrence and size of topological features within the pore space of the sandstones, as well as of the nonwetting phase fluid. We measure pore throat-body aspect ratios and coordination numbers, derived from pore-network statistics of watershed-partitioned images, as well as the Euler characteristic; and we compare these values to a novel metric based on the persistent homology analysis. Through investigation of the new experimental data, along with fresh analysis of previously published data (Herring et al., 2015), we build upon and extend previous work in two-phase images (Robins et al., 2015) to multiphase flows (i.e., three-phase images), and demonstrate utility by linking to physical experiments, providing an answer to the question: what are the important microstructural features that contribute to trapping or mobilization during capillary force-dominated fluid flows, and how can we quantify these features in one composite metric?

2. Materials and Methods

2.1. Sandstone Samples

Three sandstone types were investigated in this study: Bentheimer, Berea, and Leopard sandstones. Bentheimer sandstone and Berea sandstone have both been widely used for fluid flow studies and their

properties are reported elsewhere (Ma & Morrow, 1994; Maloney et al., 1990; Peksa et al., 2015, 2016). Leopard sandstone is less well characterized in the literature, but provides an interesting sample for comparison with Bentheimer and Berea as it has a porosity in the same range as these other samples, but an absolute permeability which is an order of magnitude smaller than these other sandstone types: Liu, Herring, Arns, et al. (2017) report lattice-Boltzman derived absolute permeability values of 0.21 and 4.25 Darcy for the Leopard and Bentheimer samples, respectively; a similar analysis results in a permeability value of 1.2 Darcy for the Berea sandstone sample investigated here.

In addition to the Bentheimer sandstone sample investigated in this study, results from another recent study of fluid flow in Bentheimer samples are also included (Herring et al., 2015). Image-based statistics for petrophysical properties of the analyzed media, including pore and throat radii and other network statistics, are included in section 3.

2.2. Quasi-Static Flow Experiments

The specifics of the experimental setup have been previously presented (Herring et al., 2017); the key components of the system and the experimental procedure are described briefly here. A sandstone rock core, approximately 4.3 mm in diameter, was wrapped laterally with two layers of hydrophilic membrane (pore size of 1.2 μm; General Electric Company, Fairfield CT, USA) and two layers of Teflon tape, and inserted into a thin-walled in-house manufactured titanium or polyether ether ketone core holder. The hydrophilic membrane layers around the core provided a water-wet boundary condition on the walls of the cores, reducing wall flow of the nonwetting phase. Another layer of hydrophilic membrane was placed at the bottom axial face of the core and compressed onto the core via an O-ring; this lower membrane prevented nonwetting phase (air) breakthrough through the core and allowed for investigation of quasi-static equilibrium conditions for a wide range of saturation values. Axial pressure was applied by screwing the top of the core holder down onto the core, with additional O-rings and a polyether ether ketone disk placed above the core to prevent shearing of the top face of the sandstone core when the core holder top was mounted. The core holder was connected via a polyether ether ketone line to a brine (1.0 M KI) reservoir syringe (controlled via syringe pump; Harvard Apparatus, Holliston, MA, USA) and pressure transducer (Keller America, Inc., Newport News, VA, USA). A small flexible air reservoir (made of loosely stretched paraffin wax) was attached to the top of the core holder; this allowed for air entry to the core at atmospheric pressure while reducing evaporation.

The entire experimental assembly was installed in the laboratory-based X-ray CT cabinet, with the core holder installed on the rotational stage. All fluid flow processes and image acquisition steps were thus conducted in situ. First, the sandstone cores were saturated with brine under vacuum; a scan was acquired of this state. Thereafter, a LabVIEW program was initiated, which alternated syringe pump pumping cycles and image acquisition: a set volume of brine was withdrawn from the core at 0.018 mL/hr, and the syringe pump was halted and the sandstone system was allowed to equilibrate for a period of 5 min prior to initiation of scan acquisition. Time frames for equilibrium were based on the time required for transducer-based pressure readings to stabilize, and in post-acquisition data inspection, we observed no interface movement (i.e., blurring) in the tomographic images. Recent studies have reported that equilibration times required for interfacial relaxation can be quite large (i.e., time frames of hours) in glass bead (Schlüter et al., 2017) and micromodel (Gray et al., 2015) systems; the lack of movement observed in this sandstone-based study may be due to a number of factors (e.g., surface roughness, level of consolidation, grain shape) potentially resulting in differences in interface pinning and stabilization.

This cycle repeated until a pressure threshold was measured via the pressure transducer; the maximum threshold value was identified during practice experiments as the value at which pressure recordings began to approximate an asymptotic increase. This selection was chosen to enable measurements at very low wetting phase saturations while reducing the risk of air breakthrough through the hydrophilic membrane. At this point, the flow was reversed and set volumes of brine were pumped into the core at 0.018 mL/hr, with the accompanying equilibration and scan acquisition periods. In this way, multiple quasi-static steps throughout primary drainage and imbibition, and sequential drainage-imbibition cycles, were captured for each sample, providing a wide range of fluid configurations for investigation. X-ray CT scan times and other experimental parameters are reported in Table 1.

Table 1
Experimental Flow and X-ray Computed Tomography (CT) Acquisition Parameters

Sample	Imbibition Flow Rate (μL/hr)	Imbibition Ca (—)	Number of Drainage-Imbibition Cycles Investigated	Capillary Pressure Measured During Acquisition of "Dry" Scan (kPa)	Analyzed Data Volume Details			CT Acquisition Parameters		
					Physical Volume (mm³)	Cylinder Diameter (mm)	Image-Measured Porosity (%)	Scan Time (min)	Energy (keV)	Voxel Resolution (μm)
Leopard	18	$10^{-7.5}$	4	58.7	91.7	4.3	17.0	98	100	3.4
Berea	18	$10^{-7.5}$	2	41.2	75.5	4.3	18.6	97	100	4.6
Bentheimer	18	$10^{-7.7}$	1	23.1	108.4	4.4	24.2	81	100	4.9
Bentheimer Herring et al. (2015)	18	$10^{-8.6}$	5[a]	N/A	87.4	5.6	18.1	approx. 10	33.3	5.8

[a] In the experiments presented in Herring et al. (2015), five separate single cycle drainage-imbibition experiments were conducted versus the sequential drainage-imbibition cycle experiments conducted at the ANU CTLab.

Capillary numbers of the imbibition process, reported in Table 1, were calculated according to equation (2):

$$Ca = \frac{\mu v}{\sigma} = \frac{\mu \left(Q/_{A \cdot \eta} \right)}{\sigma}$$ (2)

where μ is the viscosity of the wetting phase (brine); σ is the interfacial tension between nonwetting (air) and wetting (brine) phases; and v is the pore velocity of the wetting phase (brine), further calculated as Q (the volumetric flow rate of brine) divided by A (the cross-sectional area of the core) and η (sample porosity). All imbibition processes were conducted at the same flow rate (0.018 mL/hr); minor differences in the diameter and porosity of the microcore samples led to the range of capillary numbers reported in Table 1. All experiments analyzed have low capillary numbers indicating capillary-force dominated displacements.

The experimental process for the previously published Bentheimer sandstone experiments can be found in Herring et al. (2015). Beyond CT acquisition parameters, a main difference between the two sets of experiments is the nature of the flow processes. The experiments conducted at the ANU CTLab were quasi-static, consisting of many imaging and pumping steps during each drainage or imbibition process, and the series of drainage and imbibition experiments were carried out sequentially so that the impact of hysteresis on fluid distributions could be investigated. In the experiments of Herring et al. (2015), flow was continuous during each drainage and imbibition step, with scanning periods only occurring at flow process endpoints, and the cores were resaturated for every drainage-imbibition experiment (i.e., every drainage process was a primary drainage).

2.3. X-ray Tomographic Imaging and Preliminary 3-D Data Processing

Helical image acquisition was carried out via the CTLab at Australian National University using the laboratory-based 3-D X-ray CT devices developed by the Department of Applied Mathematics. Image reconstruction was accomplished via filtered backprojection, and image processing and quantification was carried out using Mango (an image processing and quantification software developed by the department of Applied Mathematics at the Australian National University); these computational tasks were facilitated by the supercomputer resources of the National Computational Infrastructure. A cylindrical subsection of the cores (excluding the core holder and hydrophilic membrane wrapping) was selected for each sample. These subsections of raw gray scale data were segmented into three phases using two-phase segmentation via an active contour segmentation routine (Sheppard et al., 2004) and image arithmetic with the "dry" image. In this series of experiments, the dry image is the image acquired at the most well-drained states of all the successive drainage processes; capillary pressure values recorded during the acquisition of the dry image are reported in Table 1. Because all experiments were conducted in situ and the cores were not removed or otherwise handled between scanning periods, the entire sequence of images was already perfectly aligned and no complicated registration process was required. The three phases identified in the final segmented data volumes were wetting fluid (X-ray attenuating brine), nonwetting fluid (air), and solid sandstone grains. Post-segmentation noise removal was implemented by converting small isolated clusters of voxels ($<1.4 \times 10^{-5}$ mm³, equivalent to a spherical pore with a radius of 15 μm) labeled as nonwetting phase to wetting phase. Euler characteristics of the nonwetting phase were measured directly on the segmented images.

The data processing routine used for Leopard, Berea, and Bentheimer samples measured in this study is contrasted with the routine used for Bentheimer sandstone samples previously analyzed by Herring et al. (2015). The images in that previous study were acquired using monochromatic synchrotron-based radiation at the Advanced Photon Source at Argonne National Laboratory; this resulted in much shorter scan time frames, but spatially less well resolved data (voxel resolution of 5.8 μm; see Table 1). The gray scale data were smoothed using a median filter, and segmented by setting the segmentation threshold at the gray scale histogram minimum value. The

differences in data quality and processing routine, and the resulting effects on the final quantification of the data, are highlighted in section 4.

3. Data Processing and Image Analysis

3.1. Watershed Partitioning and Network Statistical Analysis

The dry segmented data volumes were analyzed to compute several conventional pore space statistics for each sandstone type. The workflow for this process entails five computational steps: first, a Euclidean distance transform (EDT) was calculated on the pore space (Sheppard et al., 2006; Wildenschild & Sheppard, 2013). From the EDT, two data volumes were computed: a maximum covering sphere transform, which assigns to each point the radius largest sphere which can reside within the pore space and covers that point, and concurrently, a watershed partition, which separates the pore space into distinct labeled pore bodies (Beucher & Lantuejoul, 1979). As is common, the watershed partition overly separated the pore space (Figure 1, third row); so a subsequent region-merging step was used to reduce the number of individual labels identified in the original watershed partition (Figure 1, fourth row). This points to a disadvantage of the watershed partition (and potential subsequent region-merging): the accuracy of the pore partitioning is relatively subjective, with multiple opportunities for user input, which opens the possibility for inconsistent data analysis and comparison.

Finally, a pore network was generated using three input data volumes: the region-merged watershed partition, the EDT of the pore space, and the maximum covering sphere transform. The details of this network generation algorithm are reported in Sheppard et al. (2005). After the network was generated, statistics including distributions of pore body and throat sizes, aspect ratios, and coordination numbers were measured (on a volume-weighted basis) for each sandstone sample.

3.2. Persistent Homology Analysis of Pore Space and Nonwetting Phase

We used the software package Diamorse (Delgado-Friedrichs et al., 2015) to calculate the persistent homology signatures of data volumes; this program has been used previously to measure length scales of topologically relevant features of porous media (Liu, Herring, Robins, et al., 2017; Robins et al., 2015). This analysis can be conducted on any two-phase image; for example, the image should be segmented into pore phase versus grain phase, or nonwetting phase versus combined solid/wetting phase. We performed both types of analysis, but for simplicity, the description of the method herein is written assuming a dry image, that is, a data set containing only solid phase and pore space.

The approach is similar to a level set method: first, a signed Euclidean distance transform (SEDT) was calculated from the segmented binary image. This is identical to the EDT described above except that all voxels in both pore and grain phases are labeled with values representing the Euclidean distance to the pore-grain boundary; in the application presented here, negative values represent the pore phase and positive values in the grain phase (Figure 2b). Then, for each value that exists in the SEDT, starting with the largest negative values (i.e., the largest pore body centers) and increasing incrementally to the maximum positive value (i.e., the largest grain center), we identify changes in the topology of the level sets (Figure 2); the sequence of lower level sets is called a "filtration." The appearance of a new topological feature is termed its "birth," the disappearance of this feature is termed its "death," and the difference between the two values is the "persistence" of the feature. Using these three metrics—the level set threshold values at which features are born, die, and the difference between them—topologically relevant and dominant length scales were identified for each data set.

The results of the persistent homology analysis are visualized as histograms, where counts of topological features in each dimension of homology are plotted as a function of both birth and death level set distance values (termed "persistence diagrams"; Figure 3). In discussion of the persistence diagrams, we use the convention that the upper right quadrant (birth and death are both positive) is the first quadrant, and quadrant number increases in the counterclockwise direction (indicated by bolded numbers in Figure 3b).

Conceptual interpretation of the persistence diagrams requires clear designation of the sign of the pore phase versus grain phase in the SEDT. Pore phase β_0 features all have negative birth values (i.e., are born in the pore phase); a β_0 feature dies at the level set distance value that it merges with another β_0 feature. For β_0 features which originate in connected pore bodies, the death value will be negative (because
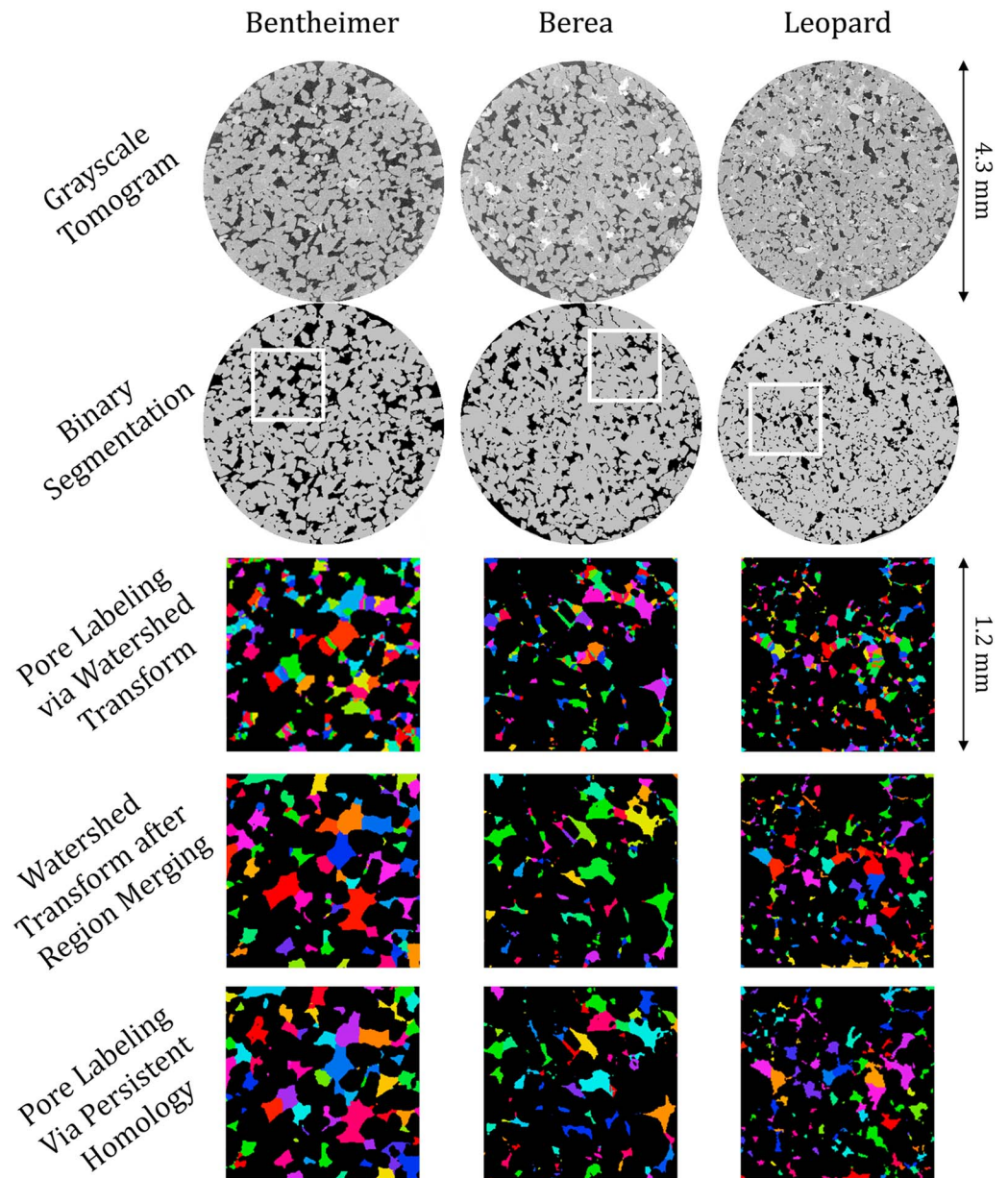
Figure 1. The 2-D slices (through the *z* dimension) of dry sandstone data volumes imaged with X-ray computed tomography (CT), and subsequent segmentation and pore labeling results. The squares on the segmented slices (second row) indicate the locations of the blown-up subsections of the pore-labeled data (third through fifth rows); in the pore-labeled images, each color represents a different pore body as identified by the indicated method.

merger with other β_0 features occurs in the pore space); in contrast, disconnected pore bodies will die in the grain phase, and the death value will be positive. For both connected and disconnected pore bodies, the birth value measures the maximal inscribed sphere radii, and so provides an estimate of the size of the largest pore in the β_0 feature. Thus, the size and occurrence of disconnected pore spaces are reported in the second quadrant of the β_0 histogram, and the size and occurrence of connected β_0 features are reported in the third quadrant (Figure 3b). The ensemble of β_0 features identified in the image thus corresponds to individually identified pore bodies present in the image (e.g., Figure 1, fourth row).

Three types of β_1 features are possible for the segmented porous media images investigated here. A "loop" which is born the pore phase (negative distance value), and that does not merge until the level set threshold has entered the solid phase (positive distance value), indicates a truly redundant pore pathway around a solid
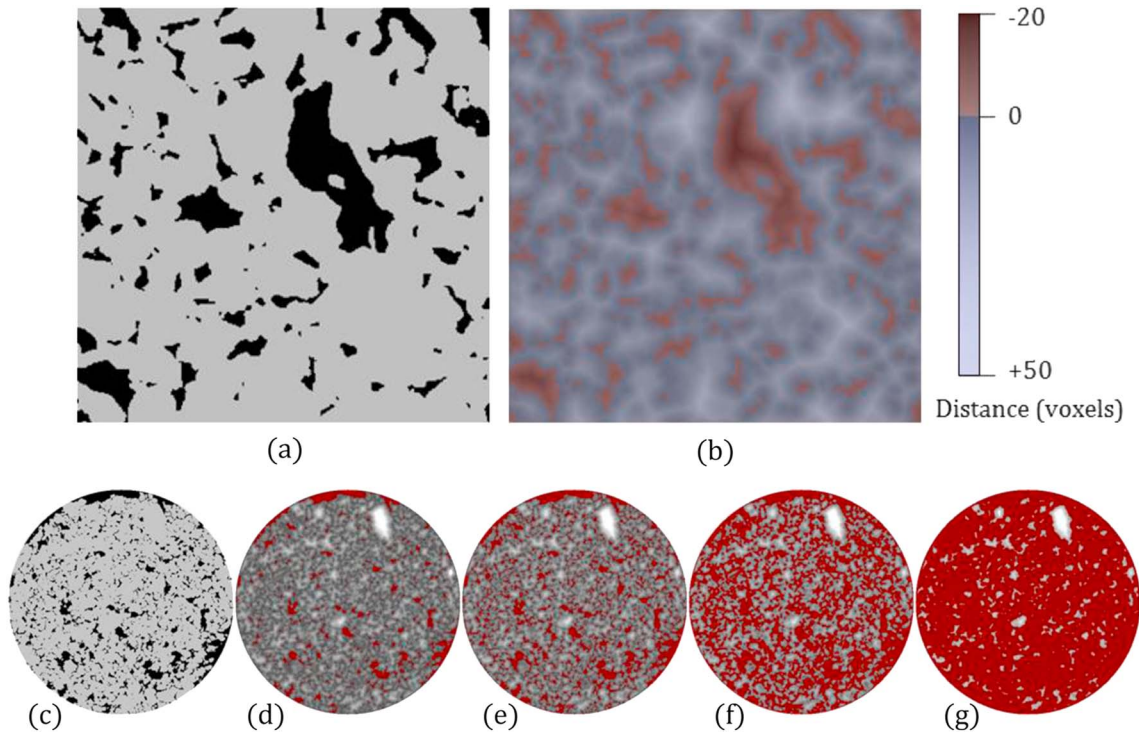
Figure 2. Example of (a) segmented data and (b) the corresponding signed Euclidean distance transform (SEDT) calculated for a 2-D subsection of leopard sandstone. In (a), black represents the pore space and gray represents solid phase; in (b), red regions indicate distance from a point in the pore space to the solid-pore interface and have a negative sign. Blue regions indicate the distance from each point in the solid phase to the solid-pore interface and are designated to be positive. The filtration process is shown for (c) a segmented 2-D slice from the vertical *z* dimension, with the progressive thresholds of the signed Euclidean distance transform shown in (d)–(g). Topological features of the level set value (indicated by dark red in (d)–(g) are calculated for each stage of the filtration process.
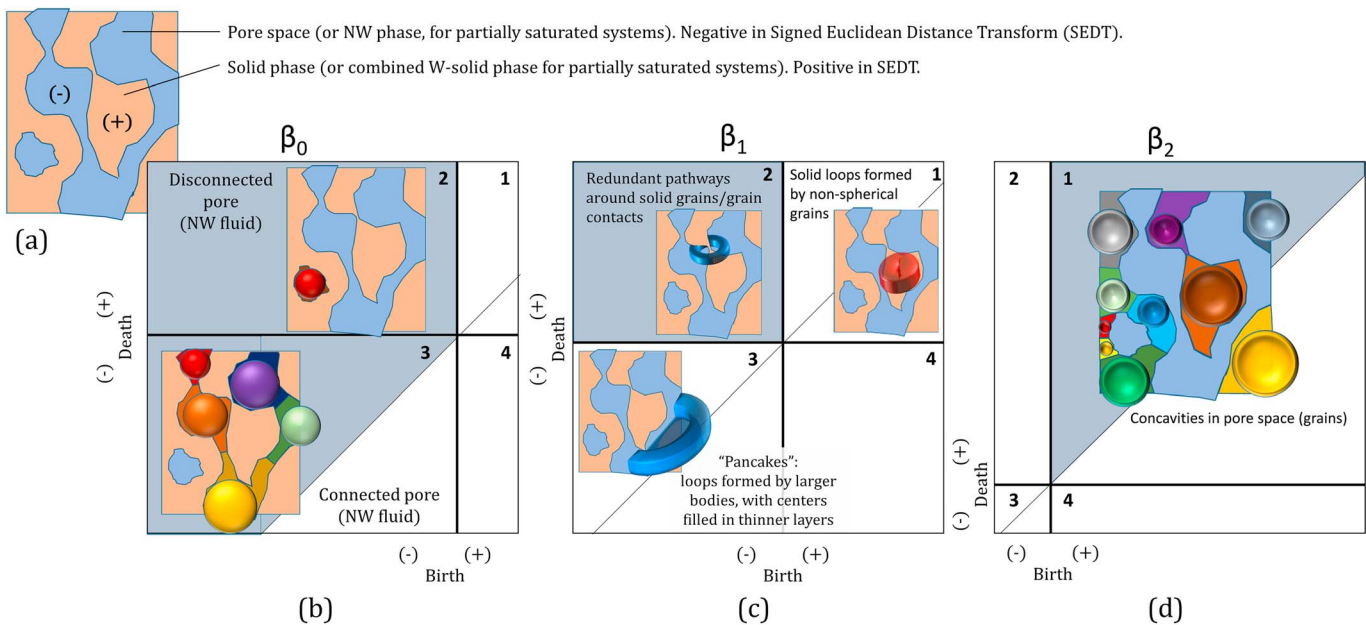

Figure 3. Illustration of (a) a 2-D subsection of an idealized porous medium, where pore space is blue (with accompanying negative distance values) and solid phase is orange (positive distance values), and (b–d) examples of persistence diagrams of β features. The birth and death level set values for each feature (i.e. whether a feature's birth and death values are in the pore space or the solid phase) indicate the physical manifestation of the feature. The two different types of β_0 features are shown in (b), the three types of β_1 features are shown in (c), and the two types of β_2 features are indicated in (d). The quadrant of the histogram which is used in calculations of pore space characterizations is shaded in (b)–(d). Bold numbers in (b)–(d) indicate the convention for quadrant labeling.

obstacle. These "true" pore space loops are reported in the second quadrant of the β_1 histogram (Figure 3c); the birth value of the loop provides the size of the narrowest throat contributing to the loop. A loop that is born in the pore space and also dies in the pore space (i.e., birth and death are both negative values) is a loop that originates in relatively large open pore bodies and merges within a thinner pore space layer spanning through the center of the loop. This applies, for example, in a region where two spherical grains nearly touch but remain slightly separated: the loop originates in the larger pore space outside of and between the grains, and dies in the open center, just between the grain contacts. These highly nonconvex β_1 features do not indicate truly redundant pathways and are reported in the third quadrant of the β_1 histogram (Figure 3c). The β_1 loops with both birth and death threshold values in the solid phase indicate grains or grain conglomerations with a nonspherical "dimpled" shape; these β_1 features are reported in the first quadrant of the β_1 histogram (Figure 3c) and are neglected from calculations regarding the pore space in this study.

In the context of filtration from the pore phase to the solid phase, β_2 features (concavities) are topological signals of grains, born as the filtration progresses into the grain phase and grains become isolated from one another. These features manifest in the first quadrant of the β_2 histogram (Figure 3d). The death value of the first-quadrant β_2 features gives an estimate of the radii of individual grains in the sample (Robins et al., 2015).

The persistence (i.e., the difference between death- and birth-level set values) of each feature gives an indication of its size, shape, and connectedness relative to other features. For example, a β_0 feature dies when it merges with another larger β_0 feature; if the two β_0 features connect through small SEDT values (e.g., two pore bodies connected through a relatively large-diameter throat), the death and birth values of the smaller β_0 feature will be similar and that feature will have a low persistence. Alternatively, if the two β_0 features are isolated and separated by the opposite phase (e.g., two isolated nonwetting phase ganglia in separate pore bodies), then the difference between death and birth values may be significantly higher, and the features will have higher persistence. For β_1 features, the concept is slightly different, because a β_1 feature dies when the loop fills in; so the persistence of a β_1 feature is a measure of the difference between the size of the obstacle that the loop encompasses and the smallest constriction that formed the loop. Thus, for β_1 features measured in geologic pore spaces, a loop that encircles a large distance throughout the sample will likely be more persistent than one which only encompasses a single grain contact.

An advantage of the persistent homology analysis is that features with very low persistence (i.e., features with birth and death distance values very close to each other) can be identified and removed. The process of removing low-persistence features is termed "simplification"; simplification reduces the impact of small features on topological metrics; that is, the persistent homology analysis produces significantly less over-partitioning of the pore space as compared to a watershed partition, with less user intervention (Figure 1). A simplification level of one voxel unit of distance was used in this study; for example, β_0, β_1, and β_2 features with one voxel persistence were removed from analysis. Applying simplification helps to address the significant uncertainty that exists in quantifying features near the resolution limit of imaging.

4. Results

Results from network statistics and persistent homology-based pore-space analyses are presented in this section. Advantages and disadvantages, as well as interpretation for each analytical method, are included. In section 4.3 we introduce a composite metric based on the persistent homology analysis, and in section 4.4, the results are considered with respect to trapping of nonwetting phase.

4.1. Network Statistics Analysis of Sample Pore Space

The results of the pore network analysis (based on watershed partitioning and subsequent region-merging of the pore space) are presented in Table 2 and Figure 4.

Pore-body and pore-throat radii histograms, measured on a volume-weighted basis (i.e., body and throat counts are normalized relative to their contribution to the pore space volume, rather than by the number of bodies and throats), are presented in Figures 4a and 4b. Bin size for all data is 2.5 μm per bin. The Leopard sandstone has a broader pore size distribution, with a large proportion (40%) of the pores made

Table 2
Structural Characteristics of Dry Samples: Pore Statistics Parameters of the Analyzed Data

| Sample | Network Statistics Via Mango (Volume-Weighted) | | | |
| | Mean Feature Radii | | Mean Aspect Ratio | Mean Coordination Number |
	Pore Body (μm)	Pore Throat (μm)		
Leopard	29.4	7.9	5.5	9.5
Berea	34.3	8.1	4.3	10.7
Bentheimer	41.3	13.0	4.4	11.2
Bentheimer Herring et al. (2015)	43.3	13.8	4.4	9.1

of small pore bodies less than 20-μm radius and the remaining proportion of pore bodies spanning up to 100-μm radius, whereas the Berea and Bentheimer sandstones approximate lognormal distributions. All sandstone types have throat size distributions which are skewed toward the smallest bin size. The Berea sandstone is notable; in that, almost 65% of the throats (on a volume basis) have throats smaller than 5.9 μm. Conversely, the Bentheimer sandstone exhibits the widest range in pore throat sizes.

Pore body-throat aspect ratios and coordination number distributions of these samples are presented in Figures 4c and 4d, respectively. Despite the variety of pore-body and pore-throat sizes present in these sandstones, the rock samples analyzed in this study have similar distributions and ranges of aspect ratios and coordination numbers. Notably, the two
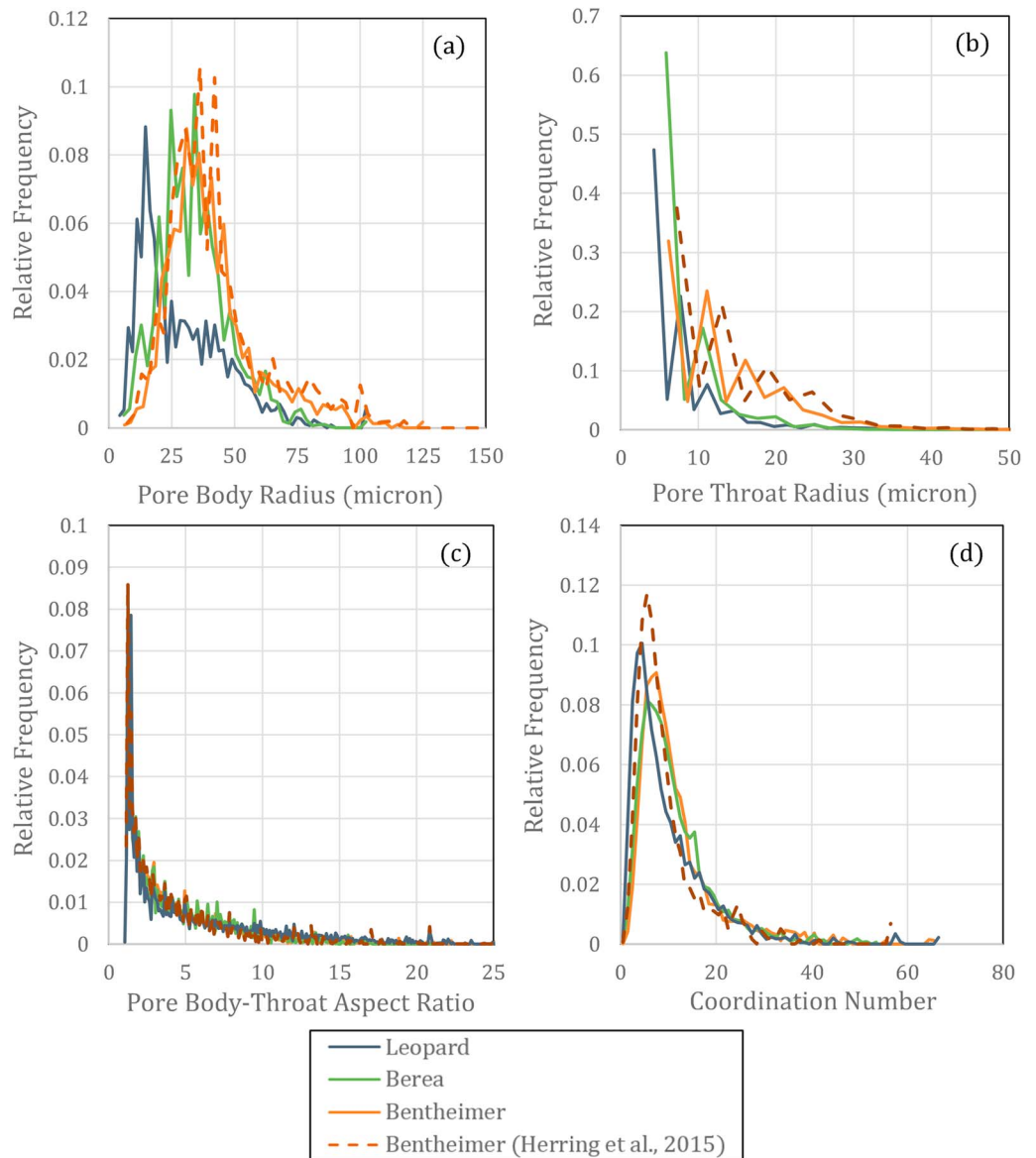

Figure 4. Pore space network statistics: Distributions measured for pore (a) body and (b) throat radii, (c) pore body-to-throat aspect ratio, and (d) coordination number. All histograms are presented on a volume-weighted basis.

sets of Bentheimer data (i.e., new experimental data from this study and the data reanalyzed from Herring et al. (2015)) exhibit the same value for mean aspect ratio, but a significant difference in mean coordination number. It is unclear whether this difference indicates a difference in rock microstructure or just reflects the sensitivity of the coordination number computation to details of the imaging and analysis. The differences in mean network statistics for the two sets of Bentheimer data demonstrate that while the differences in voxel resolution and image processing protocol do not dramatically impact average values of pore-body and throat radii sizes (differences of 5% and 6%, respectively; Table 2), there is a significant impact on pore space connectivity (i.e., approximately a 20% difference as estimated by coordination number).

4.2. Standard Topology Analysis of Pore Space and NW-Fluid Distribution

Topology of the nonwetting phase is quantified via volume-normalized Euler characteristics, as well as pore space-normalized Euler characteristics ($NW\,\widehat{\chi}_{INIT}$); both values are presented in Table 3. The pore space-normalized Euler characteristic is defined as Euler characteristic of nonwetting phase at the initial state (prior to imbibition), divided by the Euler characteristic of the pore space (originally termed the "normalized Euler characteristic" by Herring et al. (2013)). Unlike the negative-valued Euler characteristic, the pore space-normalized Euler characteristic increases with connectedness and can be positive valued (see Herring et al., 2013, 2015). Briefly, values near 1.0 indicate that nonwetting phase is very well interconnected, having invaded almost all the pore throats and creating many loops within the pore space. Negative pore space-normalized Euler characteristic values indicate that there are more disconnected nonwetting phase ganglia than redundant interconnected flow pathways within the ganglia.

4.3. Persistent Homology Analysis of Pore Space and NW-Fluid Distribution

Histograms of topological features identified by the persistent homology analysis ("persistence diagrams") are presented in Figures 5 and 6. Figure 5 shows results for the pore space of the three different sandstone types. Figure 6 shows results for nonwetting phase within Leopard sandstone at four different saturation levels.

Comparison of the persistence diagrams for the different sandstones (Figure 5) reveals complementary information to that contained in the network statistics.

Table 3
Microstructural Characteristics of Partially Saturated Samples

| Sample | | Persistent Topology Analysis | | | | Standard Topology Analysis | |
	Nonwetting Phase Saturation	Mean β_0 Birth Size (μm)	Number of β_0 Features	Mean β_1 Birth Size (μm)	Number of β_1 Features	Volume-Normalized Euler Characteristic (mm^{-3})	Pore Space-Normalized Euler Characteristic (−)
Leopard	33%	31.1	5,931	8.0	221	124	−0.19
	55%	22.6	16,002	5.7	3,135	172	−0.27
	95%	12.9	87,570	2.6	64,821	−461	0.71
	100%	12.9	87,193	2.6	65,399	−644	1
Berea	86%	23.4	19,971	5.7	15,944	−275	0.28
	94%	20.8	26,119	4.1	44,852	−886	1
Bentheimer	98%	27.1	24,622	5.9	45,752	−522	1
Bentheimer	42%	33.4	5,155	11.6	662	7	−0.02
Herring et al. (2015)	52%	34.0	6,594	12.7	919	−4	0.01
	58%	33.7	7,528	12.2	1,359	−12	0.03
	83%	29.6	13,035	9.0	7,096	−82	0.22
	88%	28.7	13,258	8.5	7,749	−89	0.29
	95%	25.1	17,572	5.3	20,656	−302	1

Note. Persistent homology analysis identifies the mean size and number of topological features (every second- and third-quadrant β_0 feature, and every second-quadrant β_1 feature measured throughout the level set filtration) of the nonwetting phase within sandstone samples for every drainage endpoint (i.e., the "initial" state prior to imbibition) for the suite of analyzed data. Standard topology values (volume-normalized Euler characteristics and normalized Euler characteristic) were measured via Mango for new experimental data of this study; for data from Herring et al. (2015), values were measured via Avizo.
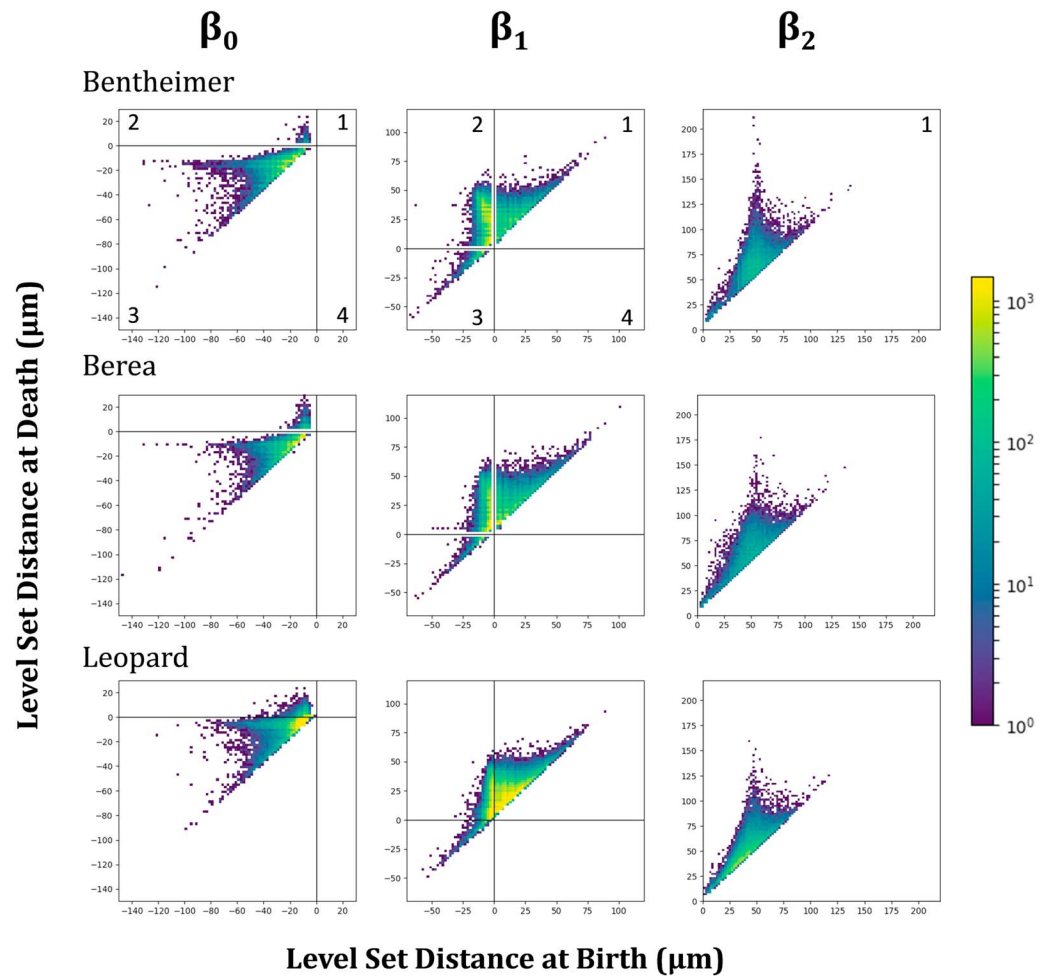
Figure 5. Persistence diagrams of topological features in the three types of "dry" sandstone samples. (top row) Convention for quadrant numbering is as indicated for the Bentheimer data.

1. The shape of the β_0 persistence diagram in the third quarter provides information on the size distribution of pore bodies (in the form of birth values), as well as the size of connections (i.e., throats) between pore bodies (indicated by the death values). The β_0 features in the second quadrant represent disconnected pore bodies.

2. The β_1 features in the second quadrant represent redundant pore-space loops, with the birth size of these features indicating the length scale of the smallest throats forming these redundant loops. This provides additional information to the throat diameter histograms derived from network statistics (Figure 4b): for flow applications, the size of individual throats is important, but also important is how the throats form redundant connections among themselves to form percolating structures.

3. Two estimates of the percolating radius of the pore space can be observed from persistence diagrams: (1) the death value of the most highly persistent third-quadrant β_0 features and (2) the birth value of the most highly persistent second-quadrant β_1 features (Robins et al., 2015). Figure 5 demonstrates that the percolating radius for Leopard is very small compared to Bentheimer and Berea.

4. The β_2 persistence diagrams provide an estimate of grain numbers and size (via the death values of β_2 features). Bentheimer sandstone has a high incidence of relatively uniformly sized grains (i.e., the "hot spot" for death values near 60 μm) and the Berea has less concentrated grain size distribution. The Leopard sandstone has large numbers of low-persistence grains, for example, the hot spot along the 1:1 line in the first quadrant, indicating that there are many small well-consolidated grains. This higher level of consolidation for Leopard as compared to Berea and Bentheimer samples is also confirmed by the larger proportion of β_1 features in the first quadrant of the Leopard persistence diagram.
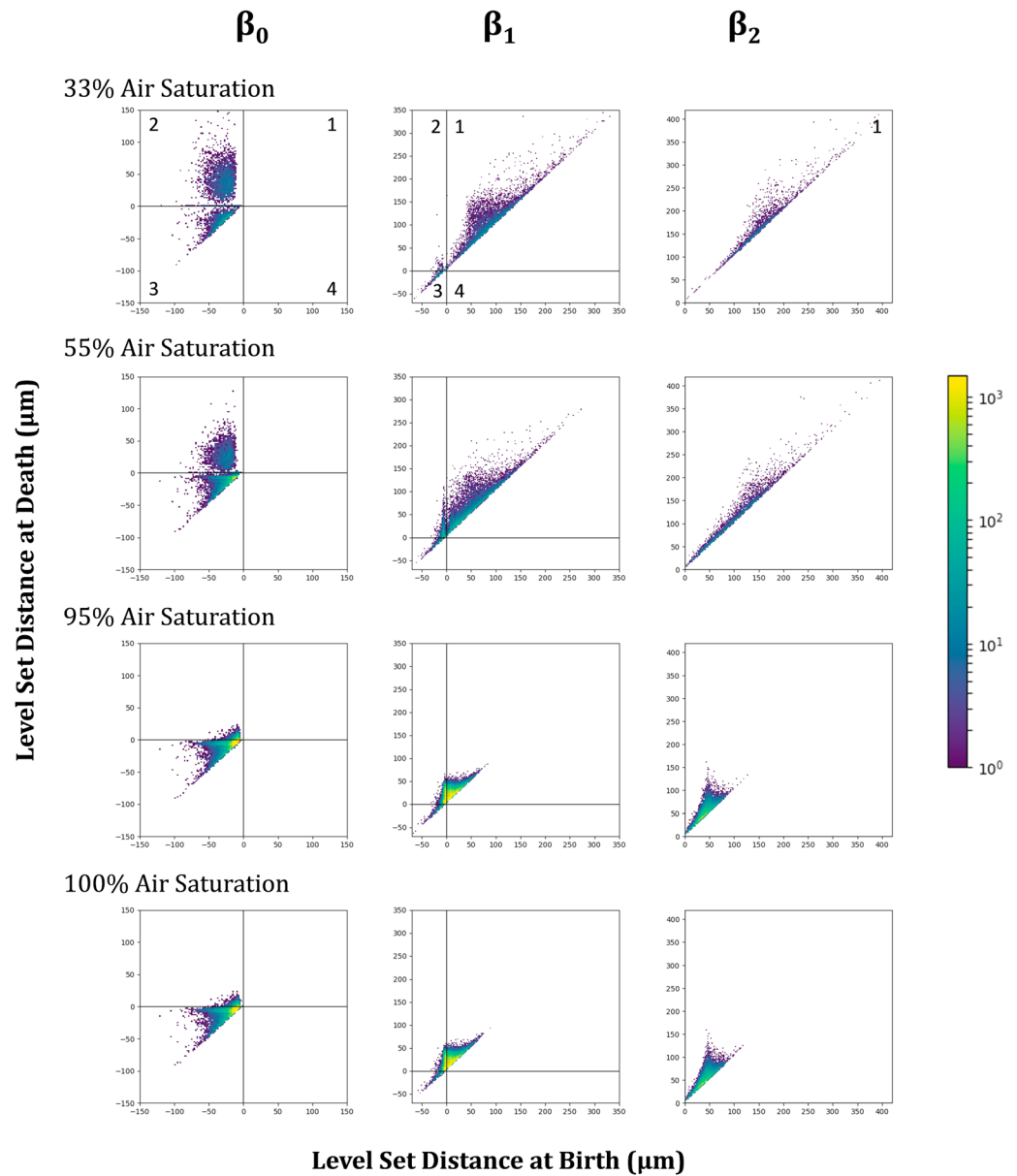
Figure 6. Persistence diagrams of topological features in leopard sandstone at four different drainage endpoints (air saturation levels). (top row) Convention for quadrant numbering is as indicated for the 33% air saturation data.

Whereas Figure 5 shows the differences in the pore space topological signatures between sandstone types, Figure 6 shows how nonwetting phase topological signatures vary for different saturation levels in Leopard sandstone. At lower nonwetting phase saturation levels (33% and 55% air saturation), there are significantly elevated numbers of disconnected nonwetting ganglia (second-quadrant β_0), and reduced numbers of connected ganglia (third-quadrant β_0). Correspondingly, there are reduced numbers of loops in the nonwetting phase (second-quadrant β_1), or nonwetting phase lenses (third-quadrant β_1) at lower saturations. It is evident that at 33% saturation the air is not percolating (i.e., no highly persistent third-quadrant β_0 features or second-quadrant β_1 features), it is close to percolating at 55%, and is definitely percolating at 95% and 100%. There are also fewer β_2 features at low saturation, as conglomerates of solid and wetting phase form larger β_2 features during the filtration process.

The information contained within the persistence diagrams can also be tabulated. Table 3 presents some of the important quantities measured for the nonwetting phase at various drainage endpoints in these

experiments, including counts and mean birth length scales associated with every second- and third-quadrant β_0 features (i.e., all pore/ganglion bodies) and every second-quadrant β_1 feature (i.e., all redundant interconnections via pore throats). For each data set, as nonwetting phase saturation increases, the counts of nonwetting phase β_0 and β_1 features increase, and the mean size of features decrease, as nonwetting phase has invaded progressively smaller pore spaces.

4.4. Persistent Homology-Based Metric

Considering the formulation of previously presented empirical metrics linked to nonwetting phase trapping —aspect ratio, coordination number, and Euler characteristic of the nonwetting phase—we use metrics measured from the persistent homology analysis to propose a new, composite metric to predict capillary trapping as a function of the microstructure of the initial nonwetting phase. The metric, defined in equation (3), quantifies the combined impacts of topology, size, and spatial distribution of nonwetting phase features which form flow mobilizing pathways relative to those which form fluid trapping pore bodies:

$$PH_{\frac{\beta_1}{\beta_0}} = \frac{\sum_i [b_i \times (d_i - b_i)]}{\sum_j [b_j \times (d_j - b_j)]} \times (voxel\ resolution)^3 \tag{3}$$

Here b is the birth threshold value (corresponding to the radius of the maximal inscribed sphere) of every topological feature, with corresponding death value d; i is the index for all β_1 features in the second quadrant of the β_1 persistence diagram; and j is the index for all β_0 features in the second and third quadrants of the β_0 persistence diagram. For the analysis presented here, any topologic feature with persistence $(d - b) \leq 1$ voxel length unit is neglected from analysis.

The $PH_{\frac{\beta_1}{\beta_0}}$ formulation incorporates the relative size of features, similarly to aspect ratio (although note that $PH_{\frac{\beta_1}{\beta_0}}$ is formulated inversely to pore body-throat aspect ratios), and as with coordination number, the $PH_{\frac{\beta_1}{\beta_0}}$ formulation incorporates information on the relative numbers of throats and bodies. Persistence is important to include in this metric, as the persistence value quantifies spatial distribution of topologic features (as described in section 3.2). By combining the influences of these geometry/connectivity/topology-based metrics, the $PH_{\frac{\beta_1}{\beta_0}}$ formulation provides a more comprehensive quantification of the relative importance of throats and pore bodies: larger, more numerous, and more persistent β_1 features (redundant pathways) result in larger $PH_{\frac{\beta_1}{\beta_0}}$ values, indicating enhanced mobilization, whereas larger, more numerous, and more persistent β_0 features lead to decreasing $PH_{\frac{\beta_1}{\beta_0}}$ values, indicating that structure facilitates capillary trapping.

Capillary trapping is a small-length-scale phenomenon, only relevant at length scales at which capillarity applies; thus, we include a measure of scale in the form of a volume unit (here chosen to be voxel resolution cubed). The choice of image voxel resolution also allows for scaling of data sets with different image resolutions.

4.5. Correlating Trapping to Microstructure

Trapping of nonwetting phase (air) was quantified for each drainage-imbibition cycle for experiments conducted in this study, as well as the Bentheimer experiments of Herring et al. (2015), and results are plotted for four previously established empirical trapping correlations in Figure 7, and for the newly derived $PH_{\frac{\beta_1}{\beta_0}}$ metric in Figure 8.

As shown, the pore space aspect ratio calculated from pore network statistics (Figure 7a) does not distinguish well between Bentheimer and Berea samples, and does not produce a robust correlation with nonwetting phase trapping efficiency $(S_{R,NW}/S_{I,NW})$, nor does the coordination number (Figure 7b) derived from the network analysis. The poor result for coordination number is due to the discrepancy in coordination numbers calculated for the two sets of Bentheimer data. While we have not been able to establish whether this difference reflects a true difference in microstructure or is an imaging artifact, the poor correlation adds weight to the argument that coordination number is not a sufficiently robust measure to be effective for predicting trapping.
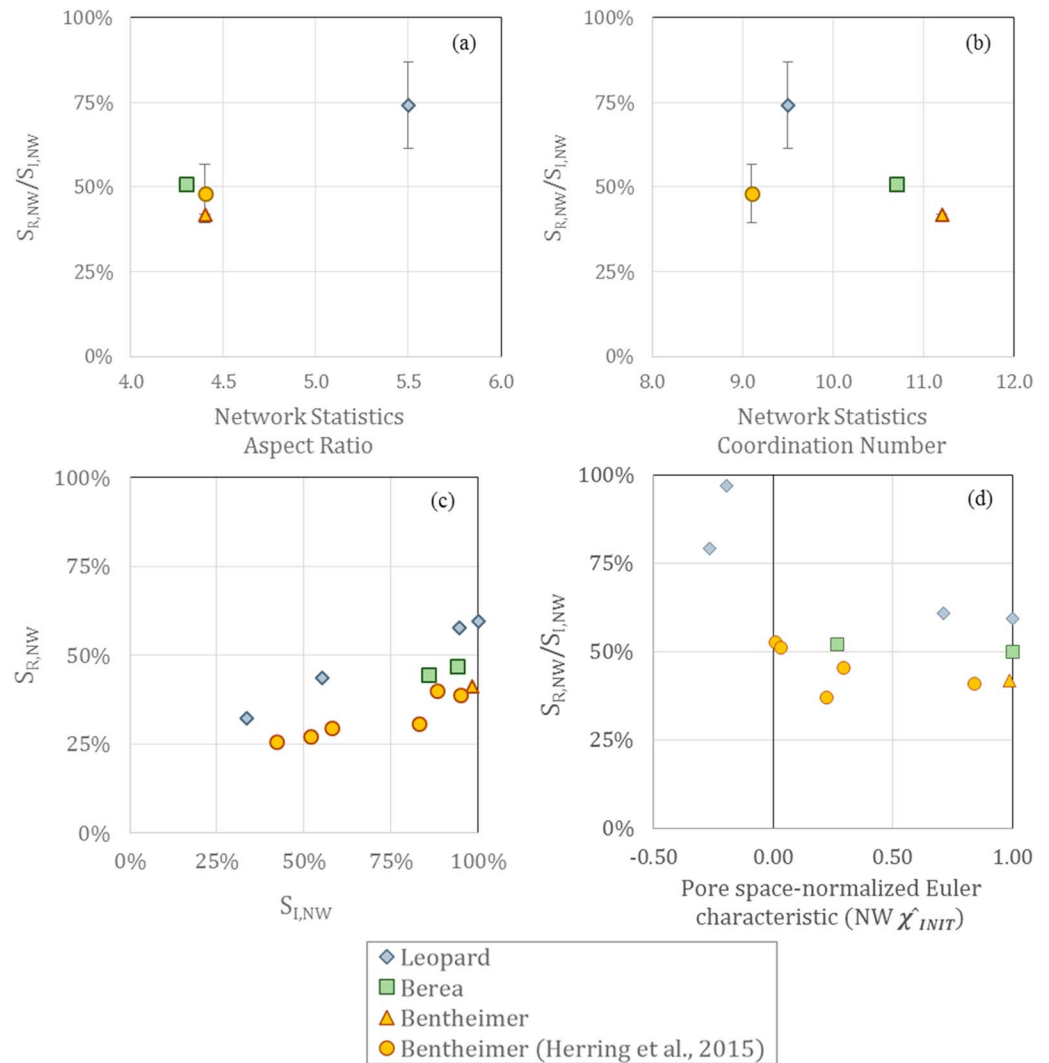
Figure 7. Four established empirical correlations for nonwetting phase trapping as a function of (a and b) pore space structure and (c and d) initial nonwetting fluid distributions. Trapping efficiency ($S_{R,NW}/S_{I,NW}$) as a function of (a) aspect ratio and (b) coordination number derived from pore networks extracted from "dry" images; error bars represent the range of trapping observed for variable initial saturation states. (c) The "trapping curve" illustrates the relationship between residual nonwetting phase saturation ($S_{R,NW}$) and initial nonwetting phase saturation ($S_{I,NW}$). (d) Trapping efficiency as a function of initial nonwetting topology, quantified by the pore space-normalized Euler number.

Figure 7c shows residual (post-imbibition, capillary trapped) air saturation ($S_{R,NW}$) plotted as a function of initial (postdrainage) air saturation ($S_{I,NW}$); this type of relationship is known as the "trapping curve" and is commonly reported in petrophysical literature (e.g., Al Mansoori et al., 2010). These results agree with previous empirical observations, but exhibit no universal relationship across sandstone types.

The relationship between initial nonwetting phase fluid topology (quantified by the pore space-normalized Euler characteristic, denoted $NW\,\widehat{\chi}_{INIT}$) and trapping efficiency is presented in Figure 7d. The relationship between nonwetting fluid topology and trapping efficiency exhibits significant differences to those measured previously (Herring et al., 2013, 2015). Herring et al. (2013) found a significant linear, negative correlation between trapping efficiency and initial nonwetting fluid topology, and Herring et al. (2015) further demonstrated that the correlation between trapping efficiency and initial nonwetting fluid topology was stronger for higher capillary number (viscosity force-dominated) displacements. The experiments analyzed in this study were all conducted under low flow rates in a capillary force-dominated regime, and so are not necessarily expected to follow the same trends observed in previous studies. Indeed, we observe no
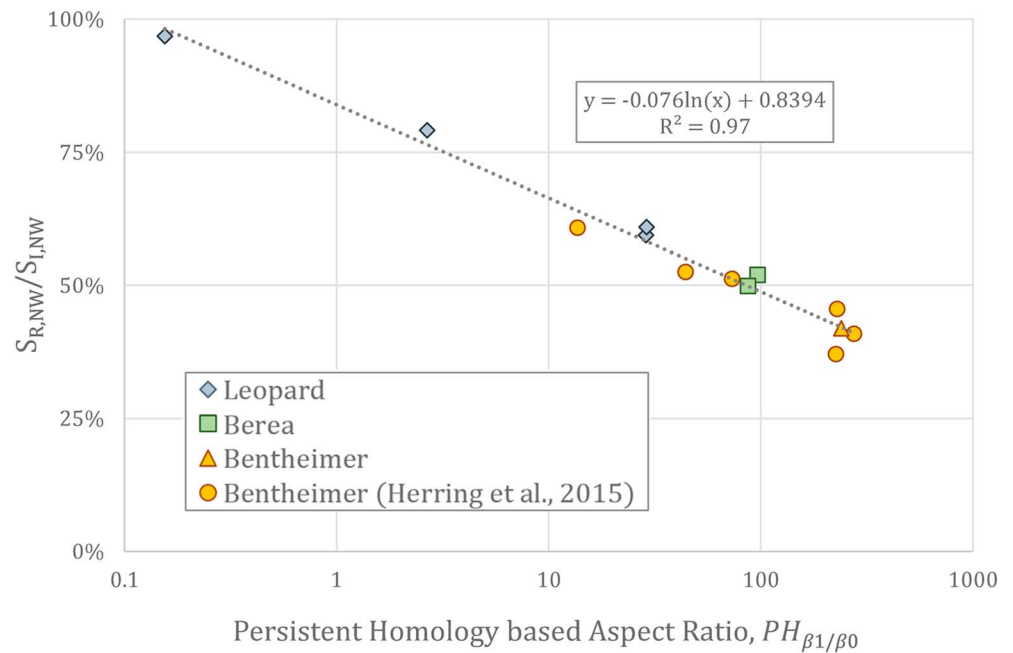
Figure 8. Trapping efficiency (residual nonwetting saturation normalized by initial nonwetting phase saturation, $S_{R,NW}/S_{I,NW}$) as a function of the persistent homology based metric $\left(PH_{\frac{\beta_1}{\beta_0}} \right)$, calculated according to equation (3) from the nonwetting phase present in each "initial" state (preimbibition) data volume.

significant negative correlation in Figure 7d. Further, Leopard sandstone samples with relatively large numbers of disconnected nonwetting bubbles (i.e., $NW \, \widehat{\chi}_{INIT} < 0$) do not exhibit a negative correlation at all. This suggests that the pore space-normalized Euler number is not a strong predictor for trapping efficiency in capillary-dominated systems, or in systems where topology is dominated by disconnected ganglia.

The persistent homology-based metric $PH_{\frac{\beta_1}{\beta_0}}$ was calculated for nonwetting phase present in each initial stage image for all sandstone types. $PH_{\frac{\beta_1}{\beta_0}}$ correlates well with trapping efficiency (Figure 8; $R^2 = 0.97$) on a semilog basis, providing a universal correlation for a wide range of saturation conditions across the three sandstone types, even for variable image voxel resolution and for the two different image processing protocols used for these samples. The applicability of the relationship relies on the incorporation of pore space measures of feature size, counts of β_0 and β_1 features, feature persistence, and length scale (voxel unit volume).

Persistent homology, like standard topological analysis, is sensitive to the presence of small features so care must be taken to remove false features (e.g., speckle noise) from segmented data. However, with respect to real features, persistent homology is more robust than standard topological analysis, because persistent homology provides an opportunity to link each feature with its size and persistence so that small features can be weighted appropriately. This robustness results in good agreement for the two sets of Bentheimer data analyzed in this study, despite the different processing routines used in preparing those data. Furthermore, the persistent homology analysis is less subject to user bias because it has fewer free parameters than pore network extraction and it is straightforward to choose consistent values for these parameters.

The relationship identified in Figure 8, in comparison to the lack of a significant relationship presented in Figure 7d, points to a key difference in fluid displacement mechanisms for capillary- versus viscous force-dominated flow processes. In viscous force-dominated flows, the initial fluid topology (i.e., the interconnectivity of the existing fluid pathways) is the key determinant of fluid trapping/mobilization as discussed in Herring et al. (2013, 2015), whereas in capillary-dominated flows the relative size of topological features is equally important. This distinction supports the two different conceptualizations of imbibition. In viscous

force-dominated imbibition, wetting fluid invades in piston-like displacements, and nonwetting fluid can be more easily mobilized if there exist many redundant pathways through which the fluid can flow in response to a pressure drop applied over a ganglia. In contrast, capillary force-dominated imbibition is pictured as a more-or-less uniform growth of wetting phase thin films on solid surfaces, where snap-off and nonwetting phase entrapment in pore bodies occurs as wetting film menisci merge at pore throats. The levels of entrapment in this regime clearly depend on the relative size of the bodies and throats containing nonwetting phase.

This understanding supports the results of many previous studies (e.g., Hughes & Blunt, 2000; Lenormand et al., 1983; Li & Wardlaw, 1986a; Wardlaw & Li, 1988, among many others). The key advance of the study presented here is the formulation of a composite metric which correlates to nonwetting phase trapping for a range of porous media, initial fluid configurations, and imaging and image processing protocols, for capillary-dominated fluid displacements.

5. Conclusions

We present the results of an experimental study investigating two-phase (air and brine) flows in Leopard, Berea, and Bentheimer sandstone types, quantified using X-ray CT while also including a previously published synchrotron CT data (Herring et al., 2015). We analyzed the CT data via three methods of quantifying structure: statistical pore network analysis; standard topology analysis (i.e., calculation of Euler characteristics); and topological persistence analysis using Diamorse, a software package developed to calculate persistent homology signatures of 3-D binary images.

We propose a new formulation for a metric derived from the persistent homology analysis, which takes into account the topology of nonwetting phase fluid as well as the size and distribution of nonwetting phase topological features (equation (3)). We compare the metrics derived from the three approaches to levels of nonwetting phase trapping observed during flow experiments (Figures 7 and 8), and demonstrate that the aspect ratio calculated from the persistent homology analysis correlates well with trapping in all systems investigated (Figure 8), encompassing a range of porous media types, saturation levels and fluid configurations, and image acquisition systems and processing routines. The observed relationship supports well-established conceptual models for nonwetting phase trapping during capillary-dominated, two-phase flow processes, while demonstrating the power of persistent homology techniques to extract critical microstructural information.

References

Al Mansoori, S. K., Itsekiri, E., Iglauer, S., Pentland, C. H., Bijeljic, B., & Blunt, M. J. (2010). Measurements of non-wetting phase trapping applied to carbon dioxide storage. *International Journal of Greenhouse Gas Control*, *4*(2), 283–288. https://doi.org/10.1016/j.ijggc.2009.09.013

Al-Raoush, R. I., & Willson, C. S. (2005). Extraction of physically realistic pore network properties from three-dimensional synchrotron X-ray microtomography images of unconsolidated porous media systems. *Journal of Hydrology*, *300*(1–4), 44–64. https://doi.org/10.1016/j.jhydrol.2004.05.005

Andrew, M., Menke, H., Blunt, M. J., & Bijeljic, B. (2015). The imaging of dynamic multiphase fluid flow using synchrotron-based X-ray microtomography at reservoir conditions. *Transport in Porous Media*, *110*(1), 1–24. https://doi.org/10.1007/s11242-015-0553-2

Armstrong, R. T., McClure, J. E., Berrill, M. A., Rücker, M., Schlüter, S., & Berg, S. (2016). Beyond Darcy's law: The role of phase topology and ganglion dynamics for two-fluid flow. *Physical Review E*, *94*(4), 043113. https://doi.org/10.1103/PhysRevE.94.043113

Bennion, D. B., & Bachu, S. (2013). The impact of interfacial tension and pore size distribution/capillary pressure character on CO_2 relative permeability at reservoir conditions in CO_2-brine systems. In *SPE/DOE Symposium on Improved Oil Recovery*. Society of Petroleum Engineers.

Beucher, S., & Lantuejoul, C. (1979). Use of watersheds in contour detection. International Real-Time Edge and Motion Detection/Estimation, Rennes.

Bultreys, T., Boone, M. A., Boone, M. N., De Schryver, T., Masschaele, B., Van Loo, D., Van Hoorebeke, L., et al. (2015). Real-time visualization of Haines jumps in sandstone with laboratory-based microcomputed tomography. *Water Resources Research*, *51*, 8668–8676. https://doi.org/10.1002/2015WR017502

Chatzis, I., Morrow, N., & Lim, H. (1983). Magnitude and detailed structure of residual oil saturation. *Old Science and Physics Education Journal*, *23*(2), 311–326.

Chatzis, I., & Morrow, N. R. (1984). Correlation of capillary number relationships for sandstone. *Science and Physics Education Journal*, *245*, 555–562.

Cheng, J.-T. (2004). Linking pressure and saturation through interfacial areas in porous media. *Geophysical Research Letters*, *31*, L08502. https://doi.org/10.1029/2003GL019282

Culligan, K. A., Wildenschild, D., Christensen, B. S. B., Gray, W. G., Rivers, M. L., & Tompson, A. F. B. (2004). Interfacial area measurements for unsaturated flow through a porous medium. *Water Resources Research*, *40*, W12413. https://doi.org/10.1029/2004WR003278

Dabaghian, Y., Mémoli, F., Frank, L., & Carlsson, G. (2012). A topological paradigm for hippocampal spatial map formation using persistent homology, edited by I. Fiete. *PLOS Computational Biology*, *8*(8), e1002581. https://doi.org/10.1371/journal.pcbi.1002581

Dalla, E., Hilpert, M., & Miller, C. T. (2002). Computation of the interfacial area for two-fluid porous medium systems. *Journal of Contaminant Hydrology*, *56*(1–2), 25–48. https://doi.org/10.1016/s0169-7722(01)00202-9

Delgado-Friedrichs, O., Robins, V., & Sheppard, A. (2015). Skeletonization and partitioning of digital images using discrete Morse theory. *IEEE Transactions on Pattern Analysis and Machine Intelligence*, *37*(3), 654–666. https://doi.org/10.1109/TPAMI.2014.2346172

Deng, W., Balhoff, M., & Cardenas, M. B. (2015). Influence of dynamic factors on nonwetting fluid snap-off in pores. *Water Resources Research*, *51*, 9182–9189. https://doi.org/10.1002/2015WR017261

Edelsbrunner, H., Letscher, D., & Zomorodian, A. (2002). Topological persistence and simplification. *Discrete & Computational Geometry*, *28*(4), 511–533. https://doi.org/10.1007/s00454-002-2885-2

Gray, W. G., Dye, A. L., McClure, J. E., Pyrak-Nolte, L. J., & Miller, C. T. (2015). On the dynamics and kinematics of two-fluid-phase flow in porous media. *Water Resources Research*, *51*, 5365–5381. https://doi.org/10.1002/2015WR016921

Herring, A. L., Andersson, L., Schlüter, S., Sheppard, A., & Wildenschild, D. (2015). Efficiently engineering pore-scale processes: Force balance and topology during nonwetting phase trapping in porous media. *Advances in Water Resources*, *79*, 91–102. https://doi.org/10.1016/j.advwatres.2015.02.005

Herring, A. L., Andersson, L., & Wildenschild, D. (2016). Enhancing residual trapping of supercritical CO_2 via cyclic injections. *Geophysical Research Letters*, *43*, 9677–9685. https://doi.org/10.1002/2016GL070304

Herring, A. L., Gilby, F. J., Li, Z., McClure, J. E., Turner, M., Veldkamp, J. P., Beeching, L., et al. (2018). Observations of nonwetting phase snap-off during drainage. *Advances in Water Resources*, *121*, 32–43. https://doi.org/10.1016/J.ADVWATRES.2018.07.016

Herring, A. L., Harper, E. J., Andersson, L., Sheppard, A., Bay, B. K., & Wildenschild, D. (2013). Effect of fluid topology on residual nonwetting phase trapping: Implications for geologic CO_2 sequestration. *Advances in Water Resources*, *62*, 47–58. https://doi.org/10.1016/j.advwatres.2013.09.015

Herring, A. L., Middleton, J., Walsh, R., Kingston, A., & Sheppard, A. (2017). Flow rate impacts on capillary pressure and interface curvature of connected and disconnected fluid phases during multiphase flow in sandstone. *Advances in Water Resources*, *107*, 460–469. https://doi.org/10.1016/j.advwatres.2017.05.011

Hughes, R. G., & Blunt, M. J. (2000). Pore scale modeling of rate effects in imbibition. *Transport in Porous Media*, *40*(3), 295–322. https://doi.org/10.1023/a:1006629019153

Kazemifar, F., Blois, G., Kyritsis, D. C., & Christensen, K. T. (2015). Quantifying the flow dynamics of supercritical CO_2–water displacement in a 2D porous micromodel using fluorescent microscopy and microscopic PIV. *Advances in Water Resources*, *95*, 352–368. https://doi.org/10.1016/j.advwatres.2015.05.011

Khanamiri, H. H., & Torsaeter, O. (2018). Fluid topology in pore scale two-phase flow imaged by synchrotron X-ray microtomography. *Water Resources Research*, *54*, 1905–1917. https://doi.org/10.1002/2017WR021302

Kim, Y., Wan, J., Kneafsey, T. J., & Tokunaga, T. K. (2012). Dewetting of silica surfaces upon reactions with supercritical CO_2 and brine: Pore-scale studies in micromodels. *Environmental Science & Technology*, *46*(7), 4228–4235. https://doi.org/10.1021/es204096w

Kimbrel, E. H., Herring, A. L., Armstrong, R. T., Lunati, I., Bay, B. K., & Wildenschild, D. (2015). Experimental characterization of nonwetting phase trapping and implications for geologic CO_2 sequestration. *International Journal of Greenhouse Gas Control*, *42*. https://doi.org/10.1016/j.ijggc.2015.07.011

Kramar, M., Levanger, R., Tithof, J., Suri, B., Xu, M., Paul, M., Schatz, M. F., et al. (2016). Analysis of Kolmogorov flow and Rayleigh-Bénard convection using persistent homology. *Physica D: Nonlinear Phenomena*, *334*, 82–89. https://doi.org/10.1016/j.physd.2016.02.003

Land, C. (1968). Calculation of imbibition relative permeability for two-and three-phase flow from rock properties. *Old Science and Physics Education Journal*, *8*(2), 149–156.

Lee, Y., Barthel, S. D., Dłotko, P., Moosavi, S. M., Hess, K., & Smit, B. (2017). Quantifying similarity of pore-geometry in nanoporous materials. *Nature Communications*, *8*, 15396. https://doi.org/10.1038/ncomms15396

Lenormand, R., Zarcone, C., & Sarr, A. (1983). Mechanisms of the displacement of one fluid by another in a network of capillary ducts. *Journal of Fluid Mechanics*, *135*(1), 337–353. https://doi.org/10.1017/S0022112083003110

Li, Y., & Wardlaw, N. C. (1986a). Mechanisms of nonwetting phase trapping during imbibition at slow rates. *Journal of Colloid and Interface Science*, *109*(2), 473–486.

Li, Y., & Wardlaw, N. C. (1986b). The influence of wettability and critical pore-throat size ratio on snap-off. *Journal of Colloid and Interface Science*, *109*(2), 461–472. https://doi.org/10.1016/0021-9797(86)90324-3

Liu, Z., Herring, A., Arns, C., Berg, S., & Armstrong, R. T. (2017). Pore-scale characterization of two-phase flow using integral geometry. *Transport in Porous Media*, *118*(1), 99–117. https://doi.org/10.1007/s11242-017-0849-5

Liu, Z., Herring, A. L., Robins, V., & Armstrong, R. T. (2017). Prediction of permeability from Euler characteristic of 3D images. In *International Symposium of the Society of Core Analysts*. Vienna, Austria.

Ma, S., & Morrow, N. R. (1994). Effect of firing on petrophysical properties of Berea sandstone. *SPE Formation Evaluation*, *9*(03), 213–218. https://doi.org/10.2118/21045-PA

Mahmud, W., & Nguyen, V. (2006). Effects of snap-off in imbibition in porous media with different spatial correlations. *Transport in Porous Media*, *64*(3), 279–300. https://doi.org/10.1007/s11242-005-4042-x

Maloney, D. R., Honarpour, M. M., & Brinkmeyer, A. D. (1990). The effects of rock characteristics on relative permeability. https://doi.org/10.2172/5086900

McClure, J. E., Berrill, M. A., Gray, W. G., & Miller, C. T. (2016). Influence of phase connectivity on the relationship among capillary pressure, fluid saturation, and interfacial area in two-fluid-phase porous medium systems. *Physical Review E*, *94*(3), 033102. https://doi.org/10.1103/PhysRevE.94.033102

Mecke, K., & Arns, C. H. (2005). Fluids in porous media: A morphometric approach. *Journal of Physics. Condensed Matter*, *17*(9), S503–S534. https://doi.org/10.1088/0953-8984/17/9/014

Mecke, K. R., & Wagner, H. (1991). Euler characteristic and related measures for random geometric sets. *Journal of Statistical Physics*, *64*(3–4), 843–850. https://doi.org/10.1007/BF01048319

Morrow, N. R., Chatzis, I., & Taber, J. T. (1988). Entrapment and mobilization of residual oil in bead packs. *SPE Reservoir Engineering*, *3*(03), 927–934. https://doi.org/10.2118/14423-PA

Nguyen, V. H., Sheppard, A. P., Knackstedt, M. A., & Val Pinczewski, W. (2006). The effect of displacement rate on imbibition relative permeability and residual saturation. *Journal of Petroleum Science and Engineering*, *52*(1–4), 54–70. https://doi.org/10.1016/j.petrol.2006.03.020

Peksa, A. E., Wolf, K.-H. A. A., Slob, E. C., Chmura, Ł., & Zitha, P. L. J. (2016). Original and pyrometamorphical altered Bentheimer sandstone; petrophysical properties, surface and dielectric behavior. *Journal of Petroleum Science and Engineering*, *149*, 270–280. https://doi.org/10.1016/j.petrol.2016.10.024

Peksa, A. E., Wolf, K.-H. A. A., & Zitha, P. L. J. (2015). Bentheimer sandstone revisited for experimental purposes. *Marine and Petroleum Geology*, *67*, 701–719. https://doi.org/10.1016/j.marpetgeo.2015.06.001

Porter, M. L., Schaap, M. G., & Wildenschild, D. (2009). Lattice-Boltzmann simulations of the capillary pressure–saturation–interfacial area relationship for porous media. *Advances in Water Resources*, *32*(11), 1632–1640. https://doi.org/10.1016/j.advwatres.2009.08.009

Porter, M. L., Wildenschild, D., Grant, G., & Gerhard, J. I. (2010). Measurement and prediction of the relationship between capillary pressure, saturation, and interfacial area in a NAPL-water-glass bead system. *Water Resources Research*, *46*, W08512. https://doi.org/10.1029/2009WR007786

Reynolds, C. A., Menke, H., Andrew, M., Blunt, M. J., & Krevor, S. (2017). Dynamic fluid connectivity during steady-state multiphase flow in a sandstone. *Proceedings of the National Academy of Sciences of the United States of America*, *114*(31), 8187–8192. https://doi.org/10.1073/pnas.1702834114

Robins, V. (1999). Towards computing homology from finite approximations. *Topology Proceedings*, *24*, 503–532.

Robins, V., Saadatfar, M., Delgado-Friedrichs, O., & Sheppard, A. P. (2015). Percolating length scales from topological persistence analysis of micro-CT images of porous materials. *Water Resources Research*, *52*, 315–329. https://doi.org/10.1002/2015WR017937

Roof, J. G. (1970). Snap-off of oil droplets in water-wet pores. *Society of Petroleum Engineers Journal*, *10*(01), 85–90. https://doi.org/10.2118/2504-PA

Rücker, M., Berg, S., Armstrong, R. T., Georgiadis, A., Ott, H., Schwing, A., Neiteler, R., et al. (2015). From connected pathway flow to ganglion dynamics. *Geophysical Research Letters*, *42*, 3888–3894. https://doi.org/10.1002/2015GL064007

Saadatfar, M., Takeuchi, H., Robins, V., Francois, N., & Hiraoka, Y. (2017). Pore configuration landscape of granular crystallization. *Nature Communications*, *8*, 15082. https://doi.org/10.1038/ncomms15082

Sanderson, N., Shugerman, E., Molnar, S., Meiss, J. D., Bradley, E., Sanderson, N., Shugerman, E., et al. (2017). Computational topology techniques for characterizing time-series data. In N. Adams, A. Tucker, & D. Weston (Eds.), *Advances in Intelligent Data Analysis XVI. IDA 2017*, *Lecture Notes in Computer Science* (pp. 284–296). Cham: Springer. https://doi.org/10.1007/978-3-319-68765-0_24

Schlüter, S., Berg, S., Li, T., Vogel, H.-J., & Wildenschild, D. (2017). Time scales of relaxation dynamics during transient conditions in two-phase flow. *Water Resources Research*, *53*, 4709–4724. https://doi.org/10.1002/2016WR019815

Schlüter, S., Berg, S., Rücker, M., Armstrong, R. T., Vogel, H.-J., Hilfer, R., & Wildenschild, D. (2016). Pore-scale displacement mechanisms as a source of hysteresis for two-phase flow in porous media. *Water Resources Research*, *52*, 2194–2205. https://doi.org/10.1002/2015WR018254

Sheppard, A. P., Sok, R. M., & Averdunk, H. (2004). Techniques for image enhancement and segmentation of tomographic images of porous materials. *Physica A: Statistical Mechanics and its Applications*, *339*(1-2), 145–151. https://doi.org/10.1016/j.physa.2004.03.057

Sheppard, A. P., Sok, R. M., & Averdunk, H. (2005). Improved pore network extraction methods.

Sheppard, A. P., Sok, R. M., Averdunk, H., Robins, V. B., & Ghous, A. (2006). Analysis of rock microstructure using high-resolution X-ray tomography. In *Proceedings of the International Symposium of the Society of Core Analysts*.

Singh, K., Menke, H., Andrew, M., Lin, Q., Rau, C., Blunt, M. J., & Bijeljic, B. (2017). Dynamics of snap-off and pore-filling events during two-phase fluid flow in permeable media. *Scientific Reports*, *7*(1), 5192. https://doi.org/10.1038/s41598-017-05204-4

Tanino, Y., & Blunt, M. J. (2012). Capillary trapping in sandstones and carbonates: Dependence on pore structure. *Water Resources Research*, *48*, W08525. https://doi.org/10.1029/2011WR011712

Vogel, H. J. (2002). Topological characterization of porous media. In K. R. Mecke & D. Stoyan (Eds.), *Morphology of Condensed Matter*, *LectureNotes in Physics* (Vol. 600, pp. 75–92). Berlin: Springer Verlag. https://doi.org/10.1007/3-540-45782-8_3

Vogel, H. J., & Kretzschmar, A. (1996). Topological characterization of pore space in soil—Sample preparation and digital image-processing. *Geoderma*, *73*(1-2), 23–38. https://doi.org/10.1016/0016-7061(96)00043-2

Vogel, H.-J., Weller, U., & Schlüter, S. (2010). Quantification of soil structure based on Minkowski functions. *Computational Geosciences*, *36*(10), 1236–1245. https://doi.org/10.1016/j.cageo.2010.03.007

Wardlaw, N. C., & Li, Y. (1988). Fluid topology, pore size and aspect ratio during imbibition. *Transport in Porous Media*, *3*(1), 17–34. https://doi.org/10.1007/bf00222684

Wildenschild, D., & Sheppard, A. P. (2013). X-ray imaging and analysis techniques for quantifying pore-scale structure and processes in subsurface porous medium systems. *Advances in Water Resources*, *51*, 217–246. https://doi.org/10.1016/j.advwatres.2012.07.018